



Quantifying spatial peat depth with seismic micronodes and the implications for carbon stock estimates

Jack B. Muir^{a,f,g,*}, Simon Jeffery^{b,e}, Joe Collins^b, Alice Marks^a, Nathan Brake^c, Tarje Nissen-Meyer^{a,d,e}

^a Department of Earth Sciences, University of Oxford, Oxford, UK

^b Centre for Crop and Environmental Sciences, Agriculture and Environment Department, Harper Adams University, Newport, UK

^c Reserve Manager - Fenn's, Whixall and Bettisfield Mosses NNR, Natural England, Whixall, UK

^d Department of Mathematics, University of Exeter, Exeter, UK

^e Earth Rover Program, London, UK

^f Research School of Earth Sciences, Australian National University, Canberra, Australia

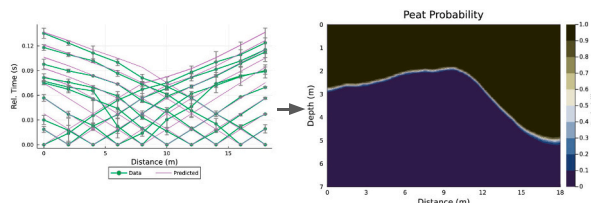
^g Fleet Space Technologies, Adelaide, Australia

HIGHLIGHTS

- Miniature seismic nodes offer excellent sensing capabilities within peatlands due to their portability and low weight.
- Level-set modelling of seismic refraction allows for infill of sparse direct probe measurements.
- Seismic data reveals variation of peat volume estimates by $\pm 20\%$ at Whixall moss, affecting the estimate of stored carbon.

GRAPHICAL ABSTRACT

Quantifying spatial peat depth with seismic micronodes and the implications for carbon stock estimates



We use seismic refraction & surface wave dispersion recorded on < 150g autonomous nodes

To estimate peat volume at high resolution, finding a $\pm 20\%$ variance from manual probes

ARTICLE INFO

Editor: Jan Vymazal

Keywords:

Peatlands
Carbon storage
Seismology
Tomography
Instrumentation

ABSTRACT

Peatlands are a major store of soil carbon, due to their high concentration of carbon-rich decayed plant material. Consequently, accurate assessment of peat volumes is important for determining land-use carbon budgets, especially in the Northern hemisphere. Determination of carbon stocks at the scale of individual peat sites has principally relied on either mechanical probing or electromagnetic geophysical methods. In this study, we investigated the use of seismic nodal instrumentation for quantifying peat depth. We used Stryde™ nodes for a deployment at the Whixall moss in Shropshire, England. We measured seismic arrival times from peat-bottom reflections, as well as dispersive surface waves to invert for a model of variable peat depth along a linear cross-section. The use of very small seismic nodes (micronodes) allows for particularly rapid deployment on challenging terrain.

* Corresponding author at: Research School of Earth Sciences, Australian National University, Canberra, Australia.

E-mail address: jack.muir@anu.edu.au (J.B. Muir).

<https://doi.org/10.1016/j.scitotenv.2024.174769>

Received 10 April 2024; Received in revised form 27 June 2024; Accepted 11 July 2024

Available online 26 July 2024

0048-9697/© 2024 The Authors. Published by Elsevier B.V. This is an open access article under the CC BY license (<http://creativecommons.org/licenses/by/4.0/>).

1. Introduction

Peatlands store an estimated 600 gigatonnes of carbon globally (Yu et al., 2011), which represents approximately a third of all soil carbon stocks (Carless et al., 2021). Most of this occurs in the northern hemisphere, between 50 and 70°N where within the boreal zone more carbon is stored in peat than is present in the above ground biomass (Beaulne et al., 2021). However, these estimates are based on several assumptions, most notably using fixed “average” values for peat depth, bulk density and accumulation history across spatially heterogeneous peat terrains, meaning there are large uncertainties; current estimates state that northern peatland stocks are in the range of 500 gigatonnes of carbon ± 100 gigatonnes (Yu, 2012).

Quantification of peat carbon stocks requires knowing the volume of peat, along with both the carbon concentration and the dry bulk density. While carbon concentration and bulk density are measurable to high levels of accuracy in the laboratory, volume is more difficult to quantify, as it requires accurate measurements of both the surface area and depth profile of a peatland. Generally, peat surface area can be mapped accurately using remote sensing (Aitkenhead, 2017; Bradley et al., 2022, e.g.) or on ground investigations, but measuring peat depth is commonly done using peat probes or corers (De Vleeschouwer et al., 2010; Parry et al., 2014, e.g.). This is labor intensive and so is costly to undertake at a high resolution and may not be feasible for studies beyond heavily monitored testbed sites. For example, Jaenicke et al. (2008) attempted to quantify carbon stocks in Indonesian peatlands. To do so they used 750 individual depth measurements which, due to the difficulties of working in peatland swamps, were generally situated near drainage canals and logging railways, potentially biasing the data and reducing the accuracy of the model.

Due to the typically strong contrast in physical properties between peat and underlying strata, geophysical imaging methods present an alternative, non-invasive method for determining peat depth. Electromagnetic methods, such as ground-penetrating radar (GPR) and electrical resistivity tomography (ERT), have frequently been used for determining peat depths (e.g. Parsekian et al., 2012; Parry et al., 2014; Comas et al., 2015; Proulx-McInnis et al., 2013; Henrion et al., 2024). However, GPR requires careful calibration against ground-truth probe data, and deploying cabled ERT and cart-based GPR instrumentation is time consuming and challenging on rough terrain. As an alternative, seismic methods are sensitive to the difference in mechanical properties between the peat and the substrate. Seismology thus provides complementary information to electromagnetic methods. Traditional near-surface seismic deployments are based on cabled geophone arrays, which suffer from similar logistical problems as cabled ERT deployments. However, recent developments in seismic instrumentation have resulted in the proliferation of seismic nodes — autonomous, cable-free units consisting of a geophone, battery, data-logger and GPS time synchronization. The size of seismic nodes has shrunk from early models with the smallest commercially available units from Stryde being 129 × 41 mm in size and 150 g in weight (for comparison, a commonly used nodal instrument for large scale deployments is the Fairfield ZLand 3C, at 163 × 117 mm, 2.8 Kg). We have generically termed the class of very small nodes as micronodes (<200 g per node, allowing >50 nodes to be reasonably carried per person). This miniaturization has democratized large-N seismic deployments, with geotechnical surveys consisting of dense 2D coverage with thousands of nodes now being routinely performed in a few days with small teams (e.g. Kiers et al., 2023). Seismic micronodes offer particular promise for the challenging setting of peatlands, as their small size and low weight allows flexible and rapid deployment. However, the particular technology mix used in extant micronode models has not yet been trialed in a peat setting. The purpose of this study was to assess their effectiveness for future large-scale peat surveys.

2. Methods

2.1. Site information

The experiment was carried out at Whixall Moss (52°55'13"N, 002°45'44"W), an ombrotrophic, raised bog that straddles the England / Wales border. The area is part of the Fenn's, Whixall & Bettisfield Mosses National Nature Reserve, which covers 1000 ha. The bog has a long history of peat extraction but has been under restoration for the past ~30 years through raising the water table the removal of trees. The majority of the bog consists of flooded peat workings, with limited raised access pathways. Vegetation within the bog is dominated by various sphagnum and cotton sedge grass. The seismic experiment was laid out along the edge of a flooded ditch, underneath the lip of a berm separating workings. Fig. 1 shows the site location in the context of the Whixall moss peat workings. Peat depth has previously been quantified across the site using peat probes to measure point depths at an approximately 100 × 100 m resolution, finding an average depth of 2.5 m (Worrall, 2022). Physical and compositional properties of the bog are contained in Table 1.

2.2. Data

The primary experiment consisted of a linear array of 10 Stryde micronodes, with a sensor spacing of 2 m. This primary array was supplemented by an additional 4 cross-line Stryde nodes and 2 cross-line GeoSIG GMS 3-channel accelerometers, however results from the cross-line instruments are not presented in this study. Stryde nodes are a new generation of portable miniaturized seismic instrumentation (Manning et al., 2018). The Stryde micronode is a single component piezoelectric accelerometer with a flat instrument response passband of 1–125 Hz. This instrument is wrapped in a water resistant polymer case, which also contains a GNSS timing system, data recorder, and battery facilities for 28 days of recording. The total dimensions of Stryde nodes are 129 mm height by 41 mm diameter, and a weight of 150 g. These nodes represent a considerable reduction in deployment effort to previous autonomous seismic instruments. The lack of cabling and low weight is ideal for the challenging deployment conditions of a peat bog. The Stryde nodes were easily coupled into the bog by simply pushing them into the upper layer of decayed organic material to the depth of the GNSS antenna. The nodes were oriented vertically, and hence record the vertical accelerations of the ground at the node locations. We employed standard near-surface geophysical surveying practice and generated seismic waves by means of repeated sledgehammer blows to a metal target plate (Milsom and Eriksen, 2013). A minimum of 3 blows were generated next to each of the deployed instruments. Due to the soft surface of the peat, the target plate sunk substantially with each blow, changing the source characteristics — however, this study used imaging methods that depended only on the timing of waves between receivers. These measurements are not substantially affected by the sinking source and are hence robust to the challenging source generation in the peat. We used the both the timings of refracted compressional waves, and the dispersion surface waves, to perform imaging using a level-set tomographic approach (Muir and Tsai, 2020).

2.3. Compressional body wave first arrivals

Seismic waves were generated from hammer blows and travelled from the source location to each receiver, where they were recorded as a set of seismograms. Using the *snuffler* subpackage of the PyRocko seismology toolbox (Heimann et al., 2017), we manually picked the initial signals of each source for all seismograms, zero-phase high-pass filtering as appropriate to remove incoherent noise. We then indexed the time of the seismograms relative to the initial signal on the seismic instrument immediately next to the source (corresponding to the hammer blow). The first arriving signals on the seismogram after the source are

compressional waves, travelling either through the ground or air. Air waves travel at the speed of sound (~ 330 m/s), which is faster than any type of wave recorded in this study; consequently we can be confident that the first arriving waves visible above the noise level on the recordings are compressional waves travelling through the soil. The first arriving compressional waves travelled either directly through the peat, or travelled as refracting head waves along the glacial till. The substantial surface wave coda of this data hid any impulsive shear-wave arrivals, so they were not utilized in this study.

Fermat's principle of least time means that the first arriving wave will travel directly through the slower peat when the source-receiver distance is short, and as a head wave through the till for longer offsets. The slope of the distance / travel-time curve will therefore change as a function of source / receiver offset, with the changeover distance giving an indication of peat interface depth. The slight delay between the hammer blow and the initial signal propagating to the receiver next to the source causes a time offset that is approximately constant for all sources; this acts as a non-zero intercept in the travel-time curve. Fig. 2 shows the recorded travel time curves, together with estimates of the picking uncertainty derived from repeated hammer blows.

2.4. Rayleigh-type surface waves

Coming behind the compressional first arrivals in the seismograms are Rayleigh waves. These waves are trapped at the surface and correspond to a mixture of compressional and shearing motion within the subsurface. A characteristic of Rayleigh waves, or more generally surface waves, is that they are dispersive in layered media, which is to say that their wave speed depends on frequency. Rayleigh waves at a certain frequency are sensitive to the geological structure above a depth of approximately $1/2$ of their wavelength (Tsai and Atiganyanun, 2014). Multiple Rayleigh modes may be present for any particular seismic

Table 1

Physical and compositional properties of the Wixhall moss (Worrall, 2022).

Moisture content	87 ± 1.48 %
Dry bulk density (0–50 cm depth)	0.07 g cm ³
Dry bulk density (50–100 cm depth)	0.55 g cm ³
Porosity	95.7 – 96.1 %
Mean organic C	48.5 ± 1.5 %
Average C budget	33 g C/m ² /yr
Age (at 91 cm depth)	861 yr

signal, each of which has their own dispersion curves that dictate the phase velocity of the mode at a given frequency. The dispersion characteristics depend on the vertical structure of the subsurface, and can be determined by array analysis. At the scale of this experiment, Rayleigh wave dispersion gives a strong constraint on the horizontally averaged structure of the medium across the array.

We derived the Rayleigh phase dispersion map in frequency–phase velocity (f – c) space using Capon's array-steering method (Capon, 1969) applied to a series of 3 hammer blows at 22 m line distance (i.e. 4 m off the end of the seismic line). Analysis of waves produced by blows past the end of the line allows Rayleigh type waves to be clearly identified in the time domain. Capon's method then optimally weighted signals across the seismic array to reduce the variance of the beam power estimate in f – c space, at the expense of potentially amplifying coherent noise signals — this allowed for the most precise analysis of the dispersive surface wave speed as a function of frequency. In our case, the hammer blow was by far the dominant signal so use of Capon's method is appropriate.

Given a set of seismograms $u_i(t)$ with Fourier transforms $\hat{u}_i(f)$, Capon's method considers the vector $\hat{u}(f) = [\hat{u}_1(f), \hat{u}_2(f), \dots, \hat{u}_n(f)]^T$. For ease of notation, we will now drop the dependence on f . For a particular c and f , the wavenumber is $k = 2\pi f/c$. The coordinate vector is $r =$

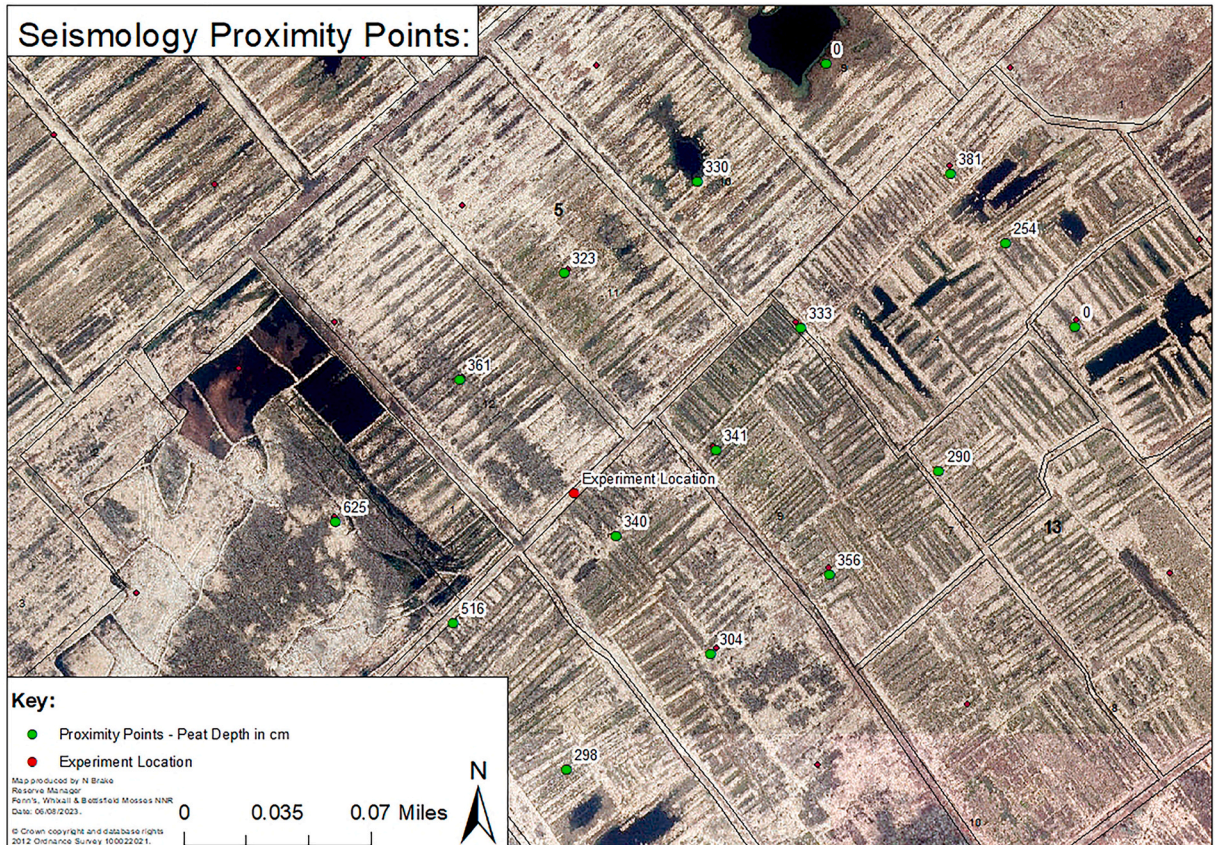


Fig. 1. Site layout, study location (in red) and measured probe depth of peat interfaces near the study area (in green).

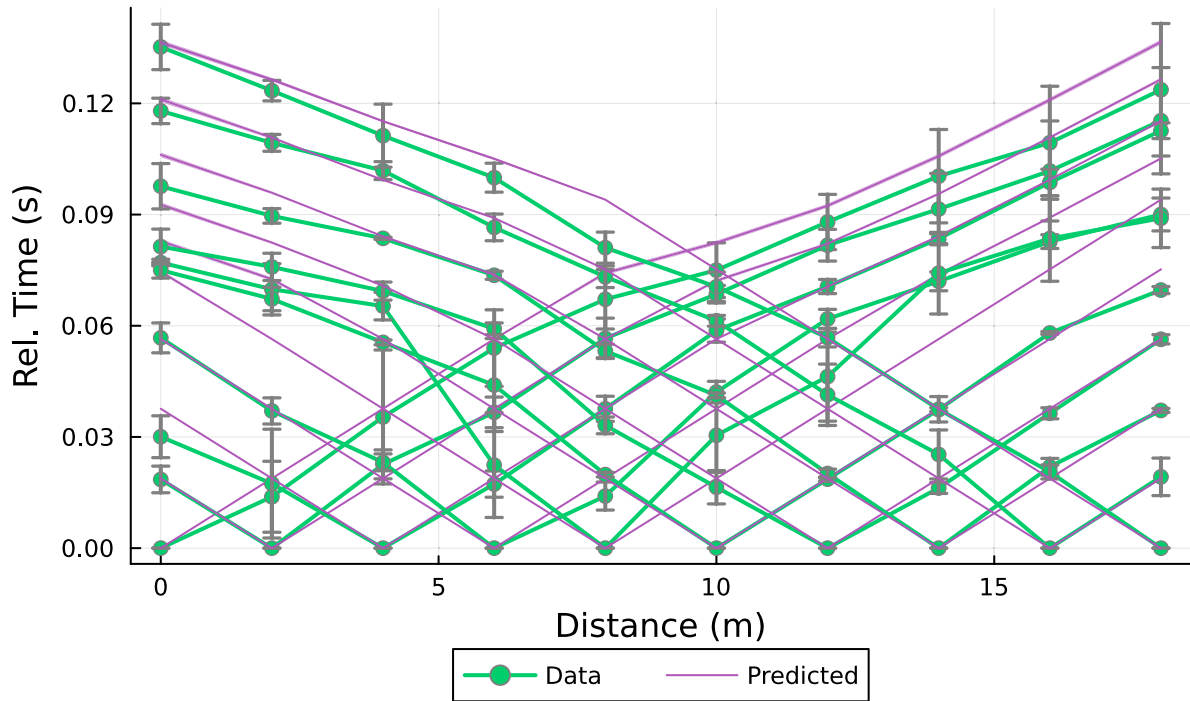


Fig. 2. Picked first arrival travel time curves relative to estimated source times, including both the estimated standard deviation from multiple shots and the correction for source time offset. Also shown are the predicted travel time curves from the final velocity model.

$[\Delta x_1, \Delta x_2, \dots, \Delta x_n]^T$, where Δx_i is the distance between some reference location and receiver i . We define the steering vector

$$a = e^{ikr}$$

(1)

and the autocorrelation matrix

$$R = \frac{\hat{u}\hat{u}^*}{|\hat{u}|^2}, \quad (2)$$

where \hat{u}^* is the Hermitian transpose of \hat{u} . Capon's estimate of beam

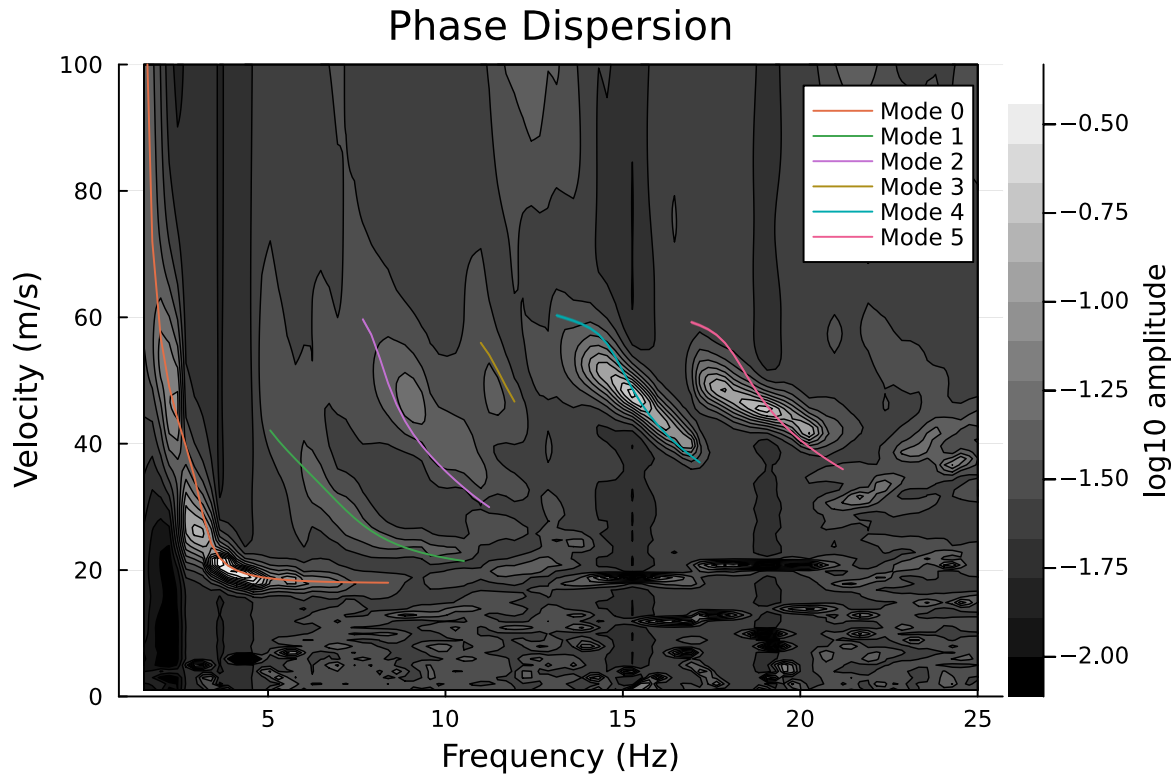


Fig. 3. Phase dispersion map obtained from Capon's array steering method, together with the predicted dispersion curves for the first 6 modes from the final velocity model.

power for phase velocity c and frequency f is then

$$P = \frac{1}{a^*(R + \lambda I)^{-1}a}, \quad (3)$$

where λ is a stabilizing regularization parameter that we set to 10^{-4} . Fig. 3 shows the resultant estimate of beam power as a function of phase velocity and frequency. The fundamental mode (mode 0) is clearly visible, with a high-frequency phase velocity of approximately $c = 17$ m/s that corresponds to Rayleigh waves travelling in the uppermost layer of the bog. Five overtones are visible in the map with varying degrees of clarity. We estimated the overtones by first masking out all parts of the dispersion map within 12 dB of the maximum beam-formed power (the 12 dB cutoff was set by manual assessment of the masked modes). The masks were labelled using the *skimage* *label* routine, and the labels corresponding to the six observed modes determined manually. We then calculated the estimated value of the dispersion curve for each mode by tracking the maximum power as a function of frequency for each mode, and the uncertainty was estimated by assuming the upper and lower bounds of the mode mask demarcate a 95 % confidence interval for the true value of a mode, to a minimum of 1 m/s error (the measurement precision of the beam-forming algorithm).

3. Imaging inversion scheme

We first derived a 1D layer-over-half-space reference model from the compressional first arrivals. The travel-time curve between source a and receiver b in such a model is given by

$$t_{ab} = t_0 + \min \left\{ \frac{\Delta x_{ab}}{v_1}, \frac{\Delta x_{ab}}{v_2} + \frac{2z\sqrt{v_2^2 - v_1^2}}{v_2 v_1} \right\}, \quad (4)$$

where v_1 and v_2 are the compressional wave velocities of the layer and the half-space, respectively, z is the thickness of the layer, Δx_{ab} and t_{ab} are the distance and travel-time between the source and receiver, and t_0 is the static correction to account for the time taken for the hammer blow to travel to the “source” recording instrument. The free parameters for the 1D layer-over-half-space model are (t_0, v_1, v_2, z) , which we fitted to the observed travel times using the *scipy* differential evolution minimizer. We can see from Eq. (4) that the mean depth to peat interface z derived from seismic imagery is in principle independent of the physical properties of the peat itself as long as v_1 and v_2 can be distinctly resolved.

After fitting the 1D reference model, we proceeded to 2D inversion using both compressional first arrivals and surface wave data. The velocity model was defined by the location of the interface between the peat and the underlying glacial till, which is parameterized by a squared-exponential Gaussian process with mean given by z , the average thickness derived above, characteristic length scale of 4 m and characteristic amplitude 0.5 m. We assumed uniform compressional wave velocity V_p within the peat and the till, and uniform shear wave velocity V_s similarly. At this scale, surface wave dispersion is only sensitive to the velocity model in an average sense, so for the purposes of predicting surface wave modes the model is laterally averaged and then extended in depth with a quadratically increasing velocity so that the modes are trapped at the surface. Further specifics of the model setup are given in the supplemental information.

We used the factored-eikonal fast-marching method (FEFMM) to model compressional first arrivals (Treister and Haber, 2016). FEFMM efficiently finds the minimum travel-time field from the source point to all other points in the domain. For each candidate 2D model, we calculated these fields for each source, extracted the predicted travel time at the other stations, and then added the source term correction t_0 to find the predicted travel time curves. To calculate surface wave dispersion we first found the horizontal average velocity model across the domain, and then employed a matrix-propagator approach using the *fast-delta* algorithm (Buchen and Ben-Hador, 1996) to predict the first

six dispersion modes over their observed frequency ranges. The forward solution operator maps candidate models into predicted data by applying these two methods.

Having defined the data, the model space, its prior, and the forward solution operator we then estimated the optimal model and its uncertainty using the Ensemble Kalman Sampling (EKS) algorithm of Garbuno-Inigo et al. (2020). EKS offers a relatively efficient way of handling physics-based problems with many free parameters when the derivative of the data in respect to the model parameters is not easily accessible (for instance when using black-box forward models, as is the case here). In EKS, we draw an initial collection of candidate models from the prior distribution. The predicted data are generated using the forward solution operators, and an approximate derivative of misfit in respect to the model parameters is found by comparing the residuals to the observed data. This derivative is used to update all of the ensemble members, which are then perturbed by additional random noise scaled by the covariance of the ensemble. The ensemble eventually converges until the derivative updates and noise additions are in equilibrium, at which point further ensemble updates sample a Gaussian approximation of the posterior distribution. EKS has previously been employed to map peat depth using electrical resistivity tomography (Tso et al., 2021), but to our knowledge this is the first investigation employing it for determining peat depth using seismic data.

4. Imaging results and discussion

Fig. 4 shows the predicted cross-section of peat probability. The depth of peat varies between 2 and 5 m, with the start of the line being in the 2–3 m range before a depression to 5 m depth on at the end of the line. The peat depth is substantively in agreement with values obtained by mechanical probing (see Supplementary Fig. 1). The depth profile was confirmed by direct probe measurement of values along the seismic line, albeit with an absolute shift in depth due to re-wetting and subsequent expansion of the peat between the initial seismic experiment and probe measurements. As the peat depths derived from this seismic survey are not calibrated against probe depth measurements, they provide an independent assessment of the peat volume which is non-invasive, spatially continuous and cost/labor efficient compared to probing, GPR or ERT methods. The areal peat estimate in this cross section is ~ 74 m², or 20 % more than the areal estimate of ~ 64 m² obtained by averaging the peat depth of the four bounding mechanical probe measurements. While it is not possible to extrapolate from this single line to an alternative peat volume for the entirety of Whixall moss, we note that a 20 % variation represents ~ 240 kilotonnes of carbon based on the mean carbon volume estimate of Natural England's BogLIFE report (which was based on probe depths coupled with two vertical profiles of carbon fraction and bulk density, Worrall, 2022).

There is increasing interest in peatland restoration for carbon sequestration, with a growing carbon credit market supported by organisations such as the IUCN-UK Peatland Code (<https://www.iucn-uk-peatlandprogramme.org/funding-finance/peatland-code>). Here, carbon credits are obtained for peatland restoration, with credit values based on avoided greenhouse gas (GHG) emissions from restored peat rather than payments for sequestered and stored carbon per se. This is because there is currently no cost effective means of accurately quantifying peat depth across the necessary scales, in a spatially explicit manner, to allow temporal monitoring. The approach presented here represents a potential means to monitor changes in carbon stocks in peatlands over time, improving our estimates of quantities of carbon being sequestered by peatland restoration, or being emitted through peatland degradation. This will facilitate effective comparison of different restoration techniques to maximize carbon sequestration, or approaches for minimizing carbon loss from degraded peatlands through improving our estimates of carbon stocks and how they change over time. Due to the vast quantities of carbon stored in peatlands worldwide, and the potentially enormous fluxes of GHG that they can

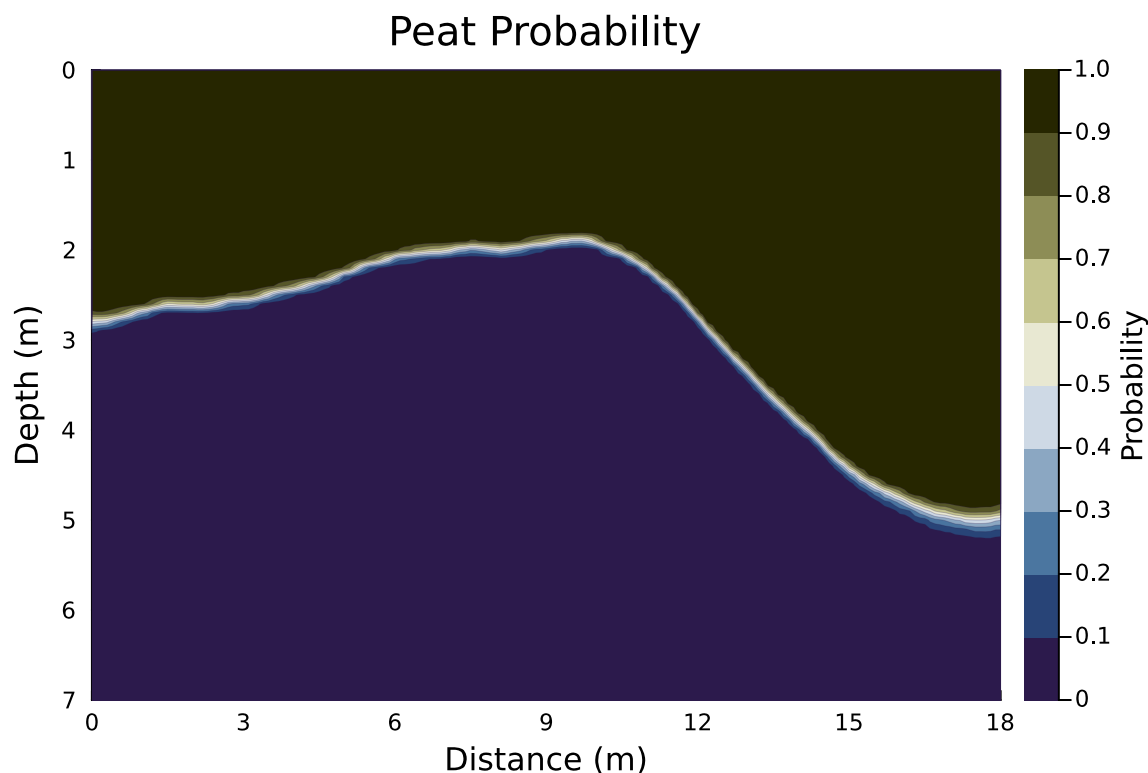


Fig. 4. Inferred probability estimate of peat within the cross-section defined by the seismic line. Stations are spaced out at 2 m intervals along the top edge.

produce, how we interact with them moving forward will have consequences for mitigating climate change. By better understanding our peat stocks we have a better chance of those consequences being positive rather than negative.

5. Conclusions

We found that micronodal seismic surveying proved to be highly effective in quantifying spatially variable peat depth. By making use of simple seismic observables (first arrival travel times and surface wave dispersion), coupled with an interface-based inversion scheme, spatial resolution at the meter scale can be achieved using this instrumental modality. The primary advantages of seismic micronodes are their flexible deployment geometry and good deployment ergonomics, stemming from their self-contained nature and low weight. These characteristics are especially pertinent to the peatland setting, where traversal of the terrain is often extremely difficult. While this was only a proof-of-concept study and so the quantitative conclusions are preliminary, we found that higher resolution peat depth maps corresponded to ~20 % variation in peat depth compared to pre-existing high-resolution mechanical probe data, which has significant implications for the total carbon budget at Whixall. Our estimates of global peat stocks are, at best, based on point measurements, inevitably with a much lower spatial resolution than available for Whixall Moss. As such, it is likely that our estimates of global C stocks in those peatlands is also subject to a high degree of error and application of the approach employed in this study will greatly improve our estimates of global peatland C stocks. Furthermore, owing to the scalable nature of this approach, it will also be possible to implement monitoring programs that quantify the changes in peat depth and hence C stocks overtime, for example in response to restoration efforts. This approach, therefore, has the potential to improve our understanding of peatland C dynamics and provide insights into how they can be used to mitigate climate change through reducing C losses and/or maximizing C sequestration.

Data accessibility and code usage

We used a custom implementation of the FEFMM algorithm available at <https://github.com/jbmuir/FEFMM.jl>, and a custom implementation of the Ensemble Kalman Sampler as described in Muir et al. (2022). The surface wave dispersion prediction used the *disba* package (Luu, 2021), which is a Python re-implementation of the Computer Programs in Seismology *surf96* code (Herrmann, 2013). Initial 1D inversion made use of *scipy* optimizing routines (SciPy 1.0 Contributors et al., 2020). Figures were created using *Plots.jl* (Breloff, 2023).

CRediT authorship contribution statement

Jack B. Muir: Writing – review & editing, Writing – original draft, Visualization, Software, Methodology, Investigation. **Simon Jeffery:** Writing – review & editing, Writing – original draft, Resources, Investigation, Conceptualization. **Joe Collins:** Resources, Investigation. **Alice Marks:** Resources, Investigation. **Nathan Brake:** Resources, Investigation. **Tarje Nissen-Meyer:** Writing – review & editing, Writing – original draft, Methodology, Investigation, Conceptualization.

Declaration of competing interest

The authors declare the following financial interests/personal relationships which may be considered as potential competing interests: Jack Muir reports financial support was provided by European Commission. Jack Muir reports a relationship with Fleet Space Technologies that includes: employment and equity or stocks. If there are other authors, they declare that they have no known competing financial interests or personal relationships that could have appeared to influence the work reported in this paper.

Data availability

Data will be made available on request.

Acknowledgements

The authors would like to thank Natural England for access to the Whixall Moss site, and Fred Worrall for providing a high-resolution version of the Whixall carbon stock assessment. JBM was supported by MSCA grant agreement no. 101027079.

Appendix A. Supplementary data

Supplementary data to this article can be found online at <https://doi.org/10.1016/j.scitotenv.2024.174769>.

References

- Aitkenhead, M.J., 2017. Mapping peat in Scotland with remote sensing and site characteristics. *Eur. J. Soil Sci.* 68 (1), 28–38. <https://doi.org/10.1111/ejss.12393> (URL <https://bsssjournals.onlinelibrary.wiley.com/doi/abs/10.1111/ejss.12393>).
- J. Beaulne, M. Garneau, G. Magnan, and É. Boucher. Peat deposits store more carbon than trees in forested peatlands of the boreal biome. *Sci. Rep.*, 11(1):2657, Jan. 2021. ISSN 2045-2322. doi: <https://doi.org/10.1038/s41598-021-82004-x>.
- Bradley, A.V., Andersen, R., Marshall, C., Sowter, A., Large, D.J., 2022. Identification of typical ecohydrological behaviours using Insar allows landscape-scale mapping of peatland condition. *Earth Surf. Dyn.* 10 (2), 261–277. <https://doi.org/10.5194/esurf-10-261-2022> (URL <https://esurf.copernicus.org/articles/10/261/2022/>).
- T. Breloff. Plots.jl. Zenodo, Aug. 2023.
- Buchen, P.W., Ben-Hador, R., Mar. 1996. Free-mode surface-wave computations. *Geophys. J. Int.* 124 (3), 869–887. <https://doi.org/10.1111/j.1365-246X.1996.tb05642.x>. ISSN 0956-540X.
- Capon, J., 1969. High-resolution frequency-wavenumber spectrum analysis. *Proc. IEEE* 57 (8), 1408–1418. <https://doi.org/10.1109/PROC.1969.7278>. ISSN 0018-9219.
- Carless, D., Kulesa, B., Booth, A., Drocourt, Y., Sinnadurai, P., Street-Perrott, F.A., Jansson, P., 2021. An integrated geophysical and GIS based approach improves estimation of peatland carbon stocks. *Geoderma* 402 (Nov.), ISSN 0016-7061.
- Comas, X., Terry, N., Slater, L., Warren, M., Kolka, R., Kristiyono, A., Sudiana, N., Nurjaman, D., Darusman, T., 2015. Imaging tropical peatlands in Indonesia using ground-penetrating radar (gpr) and electrical resistivity imaging (eri): implications for carbon stock estimates and peat soil characterization. *Biogeosciences* 12 (10), 2995–3007.
- De Vleeschouwer, F., Chambers, F.M., Swindles, G.T., 2010. Coring and sub-sampling of peatlands for palaeoenvironmental research. *Mires and peat* 7.
- Garbuno-Inigo, A., Hoffmann, F., Li, W., Stuart, A.M., Jan. 2020. Interacting Langevin diffusions: gradient structure and ensemble Kalman sampler. *SIAM J. Appl. Dyn. Syst.* 19 (1), 412–441. <https://doi.org/10.1137/19M1251655>. ISSN 1536-0040.
- Heimann, S., Kriegerowski, M., Isken, M., Cesca, S., Daout, S., Grigoli, F., Juretzek, C., Megies, T., Nooshiri, N., Steinberg, A., 2017. Pyrocko-an Open-Source Seismology Toolbox and Library.
- Henrion, M., Li, Y., Koganti, T., Bechtold, M., Jonard, F., Opfergelt, S., Vanacker, V., V. Oost, K., Lambot, S., 2024. Mapping and monitoring peatlands in the belgian hautes fagnes: insights from ground-penetrating radar and electromagnetic induction characterization. *Geoderma Reg.* 37 (0), e00795.
- R. B. Herrmann. Computer Programs in Seismology: An Evolving Tool for Instruction and Research. *Seismological Research Letters*, 84(6):1081–1088, Nov. 2013. ISSN 0895-0695, 1938-2057. doi: <https://doi.org/10.1785/0220110096>.
- Jaenicke, J., Rieley, J.O., Mott, C., Kimman, P., Siegert, F., Oct. 2008. Determination of the amount of carbon stored in Indonesian peatlands. *Geoderma* 147 (3), 151–158. <https://doi.org/10.1016/j.geoderma.2008.08.008>. ISSN 0016-7061.
- Kiers, T., Schmelzbach, C., Edme, P., Paitz, P., Amann, F., Maurer, H., Robertsson, J., Feb. 2023. Monitoring of an Alpine Landslide Using Dense Seismic Observations: Combining Distributed Acoustic Sensing and 1000 Autonomous Seismic Nodes. Technical Report EGU23-8986, Copernicus Meetings.
- K. Luu. Disba: Numba-accelerated computation of surface wave dispersion. Zenodo, Dec. 2021.
- Manning, R., Brooks, C., Ourabah, A., Popham, M., Ablyazina, D., Zhuzhel, V., Holst, E., Goujon, N., 2018. The Case for a Nimble Node, Towards a New Land Seismic Receiver System with Unlimited Channels, pp. 21–25. <https://doi.org/10.1190/segam2018-2996250.1> (URL <https://library.seg.org/doi/abs/10.1190/segam2018-2996250.1>).
- Milsom, J., Eriksen, A., 2013. *Field Geophysics*.
- Muir, J.B., Tsai, V.C., Feb. 2020. Geometric and level set tomography using ensemble Kalman inversion. *Geophys. J. Int.* 220 (2), 967–980. <https://doi.org/10.1093/gji/ggz472>. ISSN 0956-540X.
- J. B. Muir, R. W. Clayton, V. C. Tsai, and Q. Brissaud. Parsimonious velocity inversion applied to the Los Angeles Basin, CA. *J. Geophys. Res.*, 127:0 e2021JB023103, 2022. doi: <https://doi.org/10.1029/2021JB023103>.
- Parry, L., West, L., Holden, J., Chapman, P., 2014. Evaluating approaches for estimating peat depth. *J. Geophys. Res. Biogeo.* 119 (4), 567–576.
- Parsekian, A.D., Slater, L., Ntarlagiannis, D., Nolan, J., Sebesteyen, S.D., Kolka, R.K., Hanson, P.J., 2012. Uncertainty in peat volume and soil carbon estimated using ground-penetrating radar and probing. *Soil Sci. Soc. Am. J.* 76 (5), 1911–1918.
- Proulx-McInnis, S., St-Hilaire, A., Rousseau, A.N., Jutras, S., 2013. A review of ground-penetrating radar studies related to peatland stratigraphy with a case study on the determination of peat thickness in a northern boreal fen in Quebec, Canada. *Prog. Phys. Geogr.* 37 (6), 767–786.
- SciPy 1.0 Contributors, P. Virtanen, R. Gommers, T. E. Oliphant, M. Haberland, T. Reddy, D. Cournapeau, E. Burovski, P. Peterson, W. Weckesser, J. Bright, S. J. van der Walt, M. Brett, J. Wilson, K. J. Millman, N. Mayorov, A. R. J. Nelson, E. Jones, R. Kern, E. Larson, C. J. Carey, i. Polat, Y. Feng, E. W. Moore, J. VanderPlas, D. Laxalde, J. Perktold, R. Cimrman, I. Henriksen, E. A. Quintero, C. R. Harris, A. M. Archibald, A. H. Ribeiro, F. Pedregosa, and P. van Mulbregt. SciPy 1.0: Fundamental algorithms for scientific computing in Python. *Nature Methods*, 17(3):261–272, Mar. 2020. ISSN 1548-7091, 1548-7105. doi: <https://doi.org/10.1038/s41592-019-0686-2>.
- Treister, E., Haber, E., 2016. A fast marching algorithm for the factored eikonal equation. *J. Comput. Phys.* 324, 210–225.
- Tsai, V.C., Atiganyanun, S., Oct. 2014. Green's functions for surface waves in a generic velocity structure. *Bull. Seismol. Soc. Am.* 104 (5), 2573–2578. <https://doi.org/10.1785/0120140121>. ISSN 0037-1106.
- C.-H. M. Tso, M. Iglesias, P. Wilkinson, O. Kuras, J. Chambers, and A. Binley. Efficient multiscale imaging of subsurface resistivity with uncertainty quantification using ensemble Kalman inversion. *Geophysical Journal International*, 225(2):887–905, Feb. 2021. ISSN 0956-540X, 1365-246X. doi: <https://doi.org/10.1093/gji/ggab013>.
- Worrall, F., 2022. Peatland Carbon Stock Assessment of Fenn's, Whixall and Bettisfield Mosses National Nature Reserve and SAC. Technical Report LIFE15/NAT UK/000786 D3, University of Durham.
- Yu, Z., Beilman, D.W., Frolking, S., MacDonald, G.M., Roulet, N.T., Camill, P., Charman, D.J., 2011. Peatlands and their role in the global carbon cycle. *Eos, Transactions American Geophysical Union* 92 (12), 97–98. <https://doi.org/10.1029/2011EO120001>. ISSN 2324-9250.
- Yu, Z.C., Oct. 2012. Northern peatland carbon stocks and dynamics: a review. *Biogeosciences* 9 (10), 4071–4085. <https://doi.org/10.5194/bg-9-4071-2012>. ISSN 1726-4189.